36th AIAA Fluid Dynamics Conference and Exhibit
5 - 8 June 2006, San Francisco, California

AIAA 2006-3538

Direct Simulation of Subgrid Turbulence in High-Re, Wall-Bounded Flows

A. G. Gungor* and S. Menon†

School of Aerospace Engineering, Georgia Institute of Technology,
Atlanta, GA, 30332-0150, USA

The two level simulation (TLS) approach, based on the decomposition of the scales into large and small-scale components has been applied as a subgrid closure for large eddy simulation (LES) technique in order to simulate the near-wall features in high Reynolds number flows. Current LES approaches use eddy viscosity type models to evaluate the subgrid turbulence. In this proposed methodology, the subgrid turbulence is evaluated by computing the small-scale field itself rather than modeling it. The capabilities of the proposed methodology have been tested and validated for a fully developed turbulent channel flow for various Reynolds numbers. Additionally, simulation of high-Re flow past a three-dimensional bump is carried out to demonstrate the ability of this approach for complex flows. Results show that the proposed model will increase the accuracy of the LES computations without requiring a drastic increase in computational resources.

I. Introduction

ALMOST all engineering flows are turbulent, and numerical simulation of these types of flows is prohibitively expensive due to the presence of wide range of scales in both space and time. A simulation that resolves all flow scales is called direct numerical simulation (DNS) but the high computational cost of DNS makes it impractical for realistic engineering flows.

An alternative approach to DNS is the large eddy simulation (LES) technique. In LES, the computational cost is reduced by applying a low-past filter to the turbulent flow, thereby eliminating many of the small-scales below the filter width. However, the unresolved high-frequency small-scales can have a significant effect on the evolution of the resolved flow field and therefore its effect is modeled in LES using subgrid (SGS) models. The most popular approach for SGS closure is the use of an eddy viscosity closure, which appears reasonable since the small scales are supposed to be isotropic and to primarily provide dissipation for the energy transferred from the large scale.

LES is currently a most promising method for studying complex flows and has been successfully applied to many type of problems.[1] However, in the near-wall region of attached flows, the SGS modeling is a difficult problem for several reasons. First, the uniform filtering operation is ill-defined near the walls, where the filter width at a given point extends beyond the wall boundary. Second, near the wall, flow structures scale in viscous units. Hence, the near-wall resolution has to be fine enough to capture the dynamically dominant small-scales. The number of grid points required to resolve the near-wall resolved LES scales as $O(Re_\tau^2)$.[2] In addition, the small-scales in the near-wall region are strongly anisotropic. Since SGS models are derived with the assumption of small-scale isotropy, they cannot accurately represent the turbulent stresses near the wall. Consequently, for an accurate LES of wall-bounded flows, near-wall resolution comparable to that for DNS is still needed. This high resolution requirement limits the use of LES to moderate Reynolds numbers for wall-bounded shear flows.

To overcome this resolution requirement, several near-wall modeling approaches have been proposed in recent years. The objective of the near-wall modeling approach is to replace the no-slip velocity boundary conditions at the walls with approximate conditions. These conditions account for the effects of the near-wall

*Graduate Research Assistant, AIAA Student Member.
†Professor, AIAA Associate Fellow.

turbulence on the outer flow, which enable the LES to accurately capture the large-scale features away from the walls without resolving the inner layer. Examples of many near-wall models can be found in the reviews of Piomelli and Balaras[3] and Cabot and Moin.[4]

Another approach to overcome this resolution requirement is to use subgrid simulation approaches, which are based on multiscale models. Several multiscale models have been proposed in recent years, including, the Two Level Simulation (TLS) model by Kemenov and Menon,[5] the Variational Multiscale Method by Hughes *et al.*,[6,7] the Dynamic Multilevel Method by Dubois, Jaubertau and Temam,[8] and the Rapid Distortion Theory by Laval, Dubrulle and Nazarenko.[9,10] All these models are based on decomposition of the flow field into the resolved (large-scale) and unresolved (small-scale) components. From this decomposition, the coupled system of large and small-scale governing equations can be derived. In these models, small scales are explicitly simulated by solving the small-scale equations.

The new approach developed here is based on coupling the LES equations to the TLS model of Kemenov and Menon.[5,11,12,13,14] TLS model allows an explicit simulation of both the resolved and the unresolved motions. In contrast to conventional LES technique where the major effort is concentrated on modeling subgrid scale terms, in TLS the major effort is focused on modeling the small-scale velocity itself. This is acquired by decomposing the velocity field into large and small-scale components. Past studies of decaying and forced isotropic turbulence,[5,14] mixing layers[5,12,13] and fully developed channel flow[11,12,13,14] have shown that the baseline TLS model can capture important features of high-Re turbulent flows using relatively coarse grids under a wide range of conditions. In this study, TLS approach has been applied as a near-wall LES closure in order to increase accuracy of near-wall turbulence simulations without paying a DNS type of computational cost.

This paper is organized as follows. Section II discusses the governing equations of TLS and LES modeling approaches and the new subgrid turbulence simulation approach. Section III presents the results obtained by the application of the near-wall TLS-LES model for fully developed turbulent channel flow at Reynolds number based on friction velocity ranging from 590 to 2400, and for three-dimensional boundary layer flow over an axisymmetric hill at Reynolds number 130,000. Finally, Section IV summarize the conclusions and the direction for future studies.

II. Governing Equations

A. Overview of the TLS Model

Although the original TLS formulation by Kemenov and Menon[5,11,12,13,14] is for incompressible flows, to give the current TLS approach more generality, we extend it to fully compressible flows. The governing equations of motion for unsteady, compressible fluid are given as follows:

$$\begin{aligned}
\frac{\partial \rho}{\partial t} + \frac{\partial \rho u_i}{\partial x_i} &= 0 \\
\frac{\partial \rho u_i}{\partial t} + \frac{\partial}{\partial x_j}(\rho u_i u_j) &= -\frac{\partial p}{\partial x_j}\delta_{ij} + \frac{\partial \tau_{ij}}{\partial x_j} \\
\frac{\partial \rho E}{\partial t} + \frac{\partial}{\partial x_i}(\rho E u_i) &= -\frac{\partial}{\partial x_i}(p u_i) - \frac{\partial q_i}{\partial x_i} + \frac{\partial}{\partial x_i}(\tau_{ij} u_j)
\end{aligned} \tag{1}$$

where ρ is the mass density, p is the pressure, E is the total energy per unit mass, u_i is the velocity vector, q_i is the heat flux vector ($q_i = -k\frac{\partial T}{\partial x_i}$), and τ_{ij} is the viscous stress tensor ($\tau_{ij} = \mu(\frac{\partial u_i}{\partial x_j} + \frac{\partial u_j}{\partial x_i}) - \frac{2}{3}\mu\frac{\partial u_k}{\partial x_k}\delta_{ij}$).

In the TLS approach,[5,11,12,13,14] all flow variables are decomposed into large-scale (LS, superscript L) and small-scale (SS, superscript S) components as:

$$\begin{aligned}
\rho(x,t) &= \rho^L(x,t) + \rho^S(x,t), \qquad \rho u_i(x,t) = (\rho u_i)^L(x,t) + (\rho u_i)^S(x,t), \\
p(x,t) &= p^L(x,t) + p^S(x,t), \qquad \rho E(x,t) = (\rho E)^L(x,t) + (\rho E)^S(x,t) \\
u_i(x,t) &= u_i^L(x,t) + u_i^S(x,t), \qquad T(x,t) = T^L(x,t) + T^S(x,t)
\end{aligned} \tag{2}$$

Here, the LS field is obtained by applying a LS operator $L^{\triangle}$ to the total velocity, which is defined by Kemenov and Menon[5] as:

$$u_i{}^L(x) = [u_i(x)]^L = L^{\triangle} u_i(x) \tag{3}$$

Similar to decomposition given in Eq. (2), any variable can be decomposed into LS and SS components:

$$\Big((\rho u_i)^L + (\rho u_i)^S\Big)(u_j^L + u_j^S) = \Big[\Big((\rho u_i)^L + (\rho u_i)^S\Big)(u_j^L + u_j^S)\Big]^L + \Big[\Big((\rho u_i)^L + (\rho u_i)^S\Big)(u_j^L + u_j^S)\Big]^S \tag{4}$$

By substituting the decomposition given in Eq. (2) to the Navier-Stokes equations (1), the baseline TLS equations are given explicitly for both large and small scales, respectively as:

$$\begin{aligned}
\frac{\partial \rho^L}{\partial t} + \frac{\partial}{\partial x_i}(\rho u_i)^L &= F_{c,i}^S \\
\frac{\partial}{\partial t}(\rho u_i)^L + \frac{\partial}{\partial x_j}\Big((\rho u_i)^L + (\rho u_i^S)\Big)(u_j^L + u_j^S) &= -\frac{\partial p^L}{\partial x_i} + \frac{\partial \tau_{ij}^L}{\partial x_j} + F_{m,i}^S \\
\frac{\partial}{\partial t}(\rho E)^L + \frac{\partial}{\partial x_i}\Big((\rho E)^L + (\rho E)^S\Big)(u_i^L + u_i^S) &= -\frac{\partial}{\partial x_i}(p^L + p^S)(u_i^L + u_i^S) \\
-\frac{\partial q_i^L}{\partial x_i} + \frac{\partial}{\partial x_i}(\tau_{ij}^L + \tau_{ij}^S)(u_j^L + u_j^S) &+ F_{e,i}^S
\end{aligned} \tag{5}$$

$$\begin{aligned}
\frac{\partial \rho^S}{\partial t} + \frac{\partial}{\partial x_i}(\rho u_i)^S &= F_{c,i}^L \\
\frac{\partial}{\partial t}(\rho u_i)^S + \frac{\partial}{\partial x_j}\Big((\rho u_i)^L + (\rho u_i)^S\Big)(u_j^L + u_j^S) &= -\frac{\partial p^S}{\partial x_i} + \frac{\partial \tau_{ij}^S}{\partial x_j} + F_{m,i}^L \\
\frac{\partial}{\partial t}(\rho E)^S + \frac{\partial}{\partial x_i}\Big((\rho E)^L + (\rho E)^S\Big)(u_i^L + u_i^S) &= -\frac{\partial}{\partial x_i}(p^L + p^S)(u_i^L + u_i^S) \\
-\frac{\partial q_i^S}{\partial x_i} + \frac{\partial}{\partial x_i}(\tau_{ij}^L + \tau_{ij}^S)(u_j^L + u_j^S) &+ F_{e,i}^L
\end{aligned} \tag{6}$$

where, F^S and F^L are the small-scale and large-scale forcing terms. In these equations the subscript c, m and e represents the source terms in the continuity, momentum and energy equation, respectively. These forcing terms are mathematically the coupling between the large and small-scale equations and can be expressed as:

$$\begin{aligned}
F_{c,i}^L = \frac{\partial \rho^L}{\partial t} - \frac{\partial}{\partial x_i}(\rho u_i)^L \quad &, \quad F_{c,i}^S = \frac{\partial \rho^S}{\partial t} - \frac{\partial}{\partial x_i}(\rho u_i)^S \\
F_{m,i}^L = -\frac{\partial}{\partial t}(\rho u_i)^L - \frac{\partial p^L}{\partial x_i} + \frac{\partial \tau_{ij}^L}{\partial x_j} \quad &, \quad F_{m,i}^S = -\frac{\partial}{\partial t}(\rho u_i)^S - \frac{\partial p^S}{\partial x_i} + \frac{\partial \tau_{ij}^S}{\partial x_j} \\
F_{e,i}^L = -\frac{\partial}{\partial t}(\rho E)^L - \frac{\partial q_i^L}{\partial x_i} \quad &, \quad F_{e,i}^S = -\frac{\partial}{\partial t}(\rho E)^S - \frac{\partial q_i^S}{\partial x_i}
\end{aligned} \tag{7}$$

Note that, the TLS equations (5, 6) are different forms of the Navier-Stokes equations (1) written for different unknown velocities and they do not involve any type of filtering. Thus, the TLS formulation is free of the commutativity issue, which is the main restriction of LES to the wall-bounded flows and non-uniform grids. This makes TLS a viable model for all types of flows, specifically for wall-bounded flows. These features have been extensively discussed and validated in earlier studies.[5]

In order to have the same structure as the LES equations, the TLS equations can also be re-written in a different equivalent form. Substituting Eq. (4) into Eqs. (5, 6) gives another form of TLS equations as follows:

$$\begin{aligned}
\frac{\partial \rho^L}{\partial t} + \frac{\partial}{\partial x_i}(\rho u_i)^L &= G_{c,i}^S \\
\frac{\partial}{\partial t}(\rho u_i)^L + \frac{\partial}{\partial x_j}\Big[\Big((\rho u_i)^L + (\rho u_i)^S\Big)(u_j^L + u_j^S)\Big]^L &= -\frac{\partial p^L}{\partial x_i} + \frac{\partial \tau_{ij}^L}{\partial x_j} + G_{m,i}^S \\
\frac{\partial}{\partial t}(\rho E)^L + \frac{\partial}{\partial x_i}\Big[\Big((\rho E)^L + (\rho E)^S\Big)(u_i^L + u_i^S)\Big]^L &= \Big[\frac{\partial}{\partial x_i}(p^L + p^S)(u_i^L + u_i^S)\Big]^L \\
-\frac{\partial q_i^L}{\partial x_i} + \Big[\frac{\partial}{\partial x_i}(\tau_{ij}^L + \tau_{ij}^S)(u_j^L + u_j^S)\Big]^L &+ G_{e,i}^S
\end{aligned} \tag{8}$$

$$
\begin{aligned}
\frac{\partial \rho^S}{\partial t} + \frac{\partial}{\partial x_i}(\rho u_i)^S &= G^L_{c,i} \\
\frac{\partial}{\partial t}(\rho u_i)^S + \frac{\partial}{\partial x_j}\Big[\Big((\rho u_i)^L + (\rho u_i)^S\Big)(u_j^L + u_j^S)\Big]^S &= -\frac{\partial p^S}{\partial x_i} + \frac{\partial \tau_{ij}^S}{\partial x_j} + G^L_{m,i} \\
\frac{\partial}{\partial t}(\rho E)^S + \frac{\partial}{\partial x_i}\Big[\Big((\rho E)^L + (\rho E)^S\Big)(u_i^L + u_i^S)\Big]^S &= -\Big[\frac{\partial}{\partial x_i}(p^L + p^S)(u_i^L + u_i^S)\Big]^S \\
-\frac{\partial q_i^S}{\partial x_i} + \Big[\frac{\partial}{\partial x_i}(\tau_{ij}^L + \tau_{ij}^S)(u_j^L + u_j^S)\Big]^S &+ G^L_{e,i}
\end{aligned} \tag{9}
$$

Here the LS and SS forcing terms are given by:

$$
\begin{aligned}
G^L_{c,i} &= F^L_{c,i}, \qquad G^S_{c,i} = F^S_{c,i} \\
G^L_{m,i} &= F^L_{m,i} - \frac{\partial}{\partial t}(\rho u_i)^L - \frac{\partial}{\partial x_j}(\rho u_i u_j)^L, \qquad G^S_{m,i} = F^S_{m,i} - \frac{\partial}{\partial t}(\rho u_i)^S - \frac{\partial}{\partial x_j}(\rho u_i u_j)^S \\
G^L_{e,i} &= F^L_{e,i} - \frac{\partial}{\partial x_i}(\rho E u_i)^L - \frac{\partial}{\partial x_i}(p u_i)^L + \frac{\partial}{\partial x_i}(\tau_{ij} u_j)^L \\
G^S_{e,i} &= F^S_{e,i} - \frac{\partial}{\partial x_i}(\rho E u_i)^S - \frac{\partial}{\partial x_i}(p u_i)^S + \frac{\partial}{\partial x_i}(\tau_{ij} u_j)^S
\end{aligned} \tag{10}
$$

and note that both are equivalent to the original Navier-Stokes equations (1) written as[5]

$$
\begin{aligned}
G^L_{c,i} &+ G^S_{c,i} = 0 \\
G^L_{m,i} &+ G^S_{m,i} = 0 \\
G^L_{e,i} &+ G^S_{e,i} = 0
\end{aligned} \tag{11}
$$

These equations hold only when each LS and SS forcing terms are simultaneously zero (*i.e.*, $G^L_{c,i} = 0, G^S_{c,i} = 0, G^L_{m,i} = 0, G^S_{m,i} = 0, G^L_{e,i} = 0, G^S_{e,i} = 0$). If not, the small scale field obtained by solving SS equations will have contributions at the small wave numbers (i.e., at the large scales). The details and justification of these arguments are given by Kemenov and Menon.[5] By substituting Eq. (11) into the LS and the SS equations, the final form of the TLS equations can be obtained as:

$$
\begin{aligned}
\frac{\partial \rho^L}{\partial t} + \frac{\partial}{\partial x_i}(\rho u_i)^L &= 0 \\
\frac{\partial}{\partial t}(\rho u_i)^L + \frac{\partial}{\partial x_j}\Big[\Big((\rho u_i)^L + (\rho u_i^S)\Big)(u_j^L + u_j^S)\Big]^L &= -\frac{\partial p^L}{\partial x_i} + \frac{\partial \tau_{ij}^L}{\partial x_j} \\
\frac{\partial}{\partial t}(\rho E)^L + \frac{\partial}{\partial x_i}\Big[\Big((\rho E)^L + (\rho E)^S\Big)(u_i^L + u_i^S)\Big]^L &= -\Big[\frac{\partial}{\partial x_i}(p^L + p^S)(u_i^L + u_i^S)\Big]^L \\
-\frac{\partial q_i^L}{\partial x_i} + \Big[\frac{\partial}{\partial x_i}(\tau_{ij}^L + \tau_{ij}^S)(u_j^L + u_j^S)\Big]^L &
\end{aligned} \tag{12}
$$

$$
\begin{aligned}
\frac{\partial \rho^S}{\partial t} + \frac{\partial}{\partial x_i}(\rho u_i)^S &= 0 \\
\frac{\partial}{\partial t}(\rho u_i)^S + \frac{\partial}{\partial x_j}\Big[\Big((\rho u_i)^L + (\rho u_i^S)\Big)(u_j^L + u_j^S)\Big]^S &= -\frac{\partial p^S}{\partial x_i} + \frac{\partial \tau_{ij}^S}{\partial x_j} \\
\frac{\partial}{\partial t}(\rho E)^S + \frac{\partial}{\partial x_i}\Big[\Big((\rho E)^L + (\rho E)^S\Big)(u_i^L + u_i^S)\Big]^S &= -\Big[\frac{\partial}{\partial x_i}(p^L + p^S)(u_i^L + u_i^S)\Big]^S \\
-\frac{\partial q_i^S}{\partial x_i} + \Big[\frac{\partial}{\partial x_i}(\tau_{ij}^L + \tau_{ij}^S)(u_j^L + u_j^S)\Big]^S &.
\end{aligned} \tag{13}
$$

Even though the TLS approach is free from issues associated with commutation errors, it is still computationally expensive for high Reynolds number flows. Solving the full TLS equations (12, 13) is equivalent to performing DNS, and therefore, additional simplifications and modeling are necessary to reduce the overall cost of simulating the small-scale equations. Modeling small-scale equation and numerical implementation of the model are given in detail in the following sections.

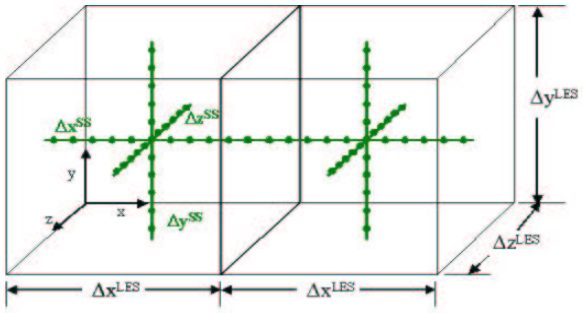

Figure 1. One dimensional TLS lines imbedded in an LES control volume.

1. *Modeling Small Scale Equations*

In the TLS model, both resolved and unresolved motions are explicitly simulated. If this simulation is done in three dimension, this method is no different from DNS, and hence it will be computationally too expensive for complex flows. To reduce the computational cost and still keep the feasibility of the model, the small-scale field is simulated in a reduced dimensional form using a modeled version of the SS equation.

In the TLS model, the small-scale field u_i^S are solved on three one dimensional lines embedded in the three-dimensional domain shown in Fig. 1, such that $u_i^S = u_i^S(s_l,t)e_i^l = u_{i,l}^S e_i^l$, where $i = 1,2,3$; $l = 1,..,N$, where N is the total number of one-dimensional lines, s_l is the coordinate along the line and e_i^l is the unit base vector of that line. Although lines can be in any shape, in this study for channel flow simulations, the small-scale lines are orthogonal to the corresponding LS coordinates as shown in Fig. 1, and for the three-dimensional bump flow simulation, these lines are body fitted lines which follow the shape of the geometry. Applying this to SS Eq. (13) leads to the simplified form of the small-scale equation on each line l_k:

$$\begin{aligned}
\frac{\partial \rho^S}{\partial t} + \frac{\partial}{\partial x_i}(\rho u_{i,l} e_i^l)^S &= 0 \\
\frac{\partial}{\partial t}(\rho u_{i,l} e_i^l)^S + \frac{\partial}{\partial x_j}\Big[\Big((\rho u_i)^L + (\rho u_{i,l} e_i^l)^S\Big)(u_j^L + (u_{j,l} e_j^l)^S)\Big]^S &= -\frac{\partial p^S}{\partial x_i} + \frac{\partial \tau_{ij}^S}{\partial x_j} \\
\frac{\partial}{\partial t}(\rho E)^S + \frac{\partial}{\partial x_i}\Big[\Big((\rho E)^L + (\rho E)^S\Big)(u_i^L + (u_{i,l} e_i^l)^S)\Big]^S &= -\Big[\frac{\partial}{\partial x_i}(p^L + p^S)(u_i^L + (u_{i,l} e_i^l)^S)\Big]^S \\
-\frac{\partial q_i^S}{\partial x_i} + \Big[\frac{\partial}{\partial x_i}(\tau_{ij}^L + \tau_{ij}^S)(u_j^L + (u_{j,l} e_j^l)^S)\Big]^S &
\end{aligned} \tag{14}$$

Reducing the SS fields on to the three one-dimensional lines is computationally more efficient; however, this reduction brings couple of problems to the numerical implementation of the SS equation. For a given line, the first and second order derivatives orthogonal to each of the line direction are unknown and have to be modeled. The model assumptions and their justifications for these terms are given in detail by Kemenov and Menon.[5] Here, for completeness, we summarize the key features of these assumptions.

For a given line l_k,

(i) the SS second order derivative along the line is equal to the averaged sum of the SS second derivatives along all three orthogonal directions:[5]

$$\frac{\partial^2 u_i^S}{\partial x_k^2} = \frac{1}{3}\sum_j \frac{\partial^2 u_i^S}{\partial x_j^2}, \qquad i,k = 1,2,3 \tag{15}$$

(ii) the convective derivatives of the SS velocity in the transverse directions to the line are neglected:[5]

$$\frac{\partial}{\partial x_j}\Big[(u_j^S + u_j^L)(u_i^S + u_i^L)\Big]^S = \frac{\partial}{\partial x_j}\Big[(u_j^S(l_k) + u_j^L)(u_i^S(l_k) + u_i^L)\Big]^S. \tag{16}$$

Further analysis of these assumptions for more complex geometries will be the subject of future studies.

If the SS lines are oriented with the LS grid, then these SS equations (14) become particularly simple and boundary conditions for SS equations can be imposed at the three-dimensional domain boundaries.

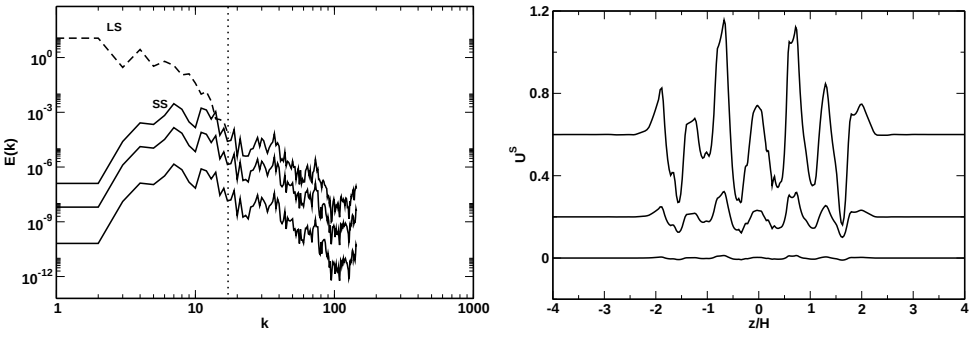

(a) (b)

Figure 2. Evolution of the SS spectral energy (a) and the SS velocity (b) along a near-wall spanwise line ($x/H = 0.5$) in three-dimensional bump. LS grid resolution is shown by dotted vertical line.

2. Numerical Implementation

Numerical implementation of the TLS equations is based on integration of LS equation and coupling the SS dynamics on the LS grid. The key point of the coupling is done by assuming that the knowledge of the SS field is only important at the LS time in order to close the LS equation. This is similar to the classical LES approach closure of the SGS terms. The detailed information of the numerical implementation can be found elsewhere.[11,12,13] Here, for completeness, the four main steps of the numerical implementation of TLS equations summarized as follows: First, at a given time step, the LS field on each 1D SS line is approximated by linear interpolation of the LS field. Then, the SS field on each line is evolved from zero initial condition and corresponding boundary condition until the SS energy matches with the LS energy near the grid scale cut off. This is illustrated in Fig. (2), where evolution of the SS spectral energy and the SS velocity are shown for a spanwise line located at $x/H = 0.5$ for three consecutive instants of time. Using the SS field, the unclosed terms $u_i^S u_j^S, u_i^S u_i^L$ and $u_j^S u_i^L$ in the LS equation are calculated on the LS grid by averaging over the lines intersecting at the LS grid point. Finally, the LS velocity is advanced to the next time level $t_{n+1}^L = t_n^L + \Delta t^L$ by integrating the LS equation using a conventional three-dimensional finite-volume scheme.

B. Overview of the LES Model

In the conventional LES, the flow variables are decomposed into large-scale (resolved-denoted by an over bar) and small-scale (SGS) (unresolved) components by applying a filtering operation,

$$\overline{f}(x,t) = \int f(x',t) G_f(x, x' : \overline{\Delta}) dx' \tag{17}$$

where, G_f is the filter function and $\overline{\Delta}$ is the filter width. From this definition, the Favre filtered variable is given as $\widetilde{f} = \overline{\rho f}/\overline{\rho}$ for the compressible approach. Applying this filtering operation to the Navier-Stokes equations and assuming that the filter commutes with differentiation, the general form of the LES equations in the Favre filtered form are obtained:

$$\begin{aligned}
\frac{\partial \overline{\rho}}{\partial t} &= -\frac{\partial \overline{\rho} \widetilde{u}_i}{\partial x_i} \\
\frac{\partial \overline{\rho}\, \widetilde{u}_i}{\partial t} &= -\frac{\partial}{\partial x_j}[\overline{\rho} \widetilde{u}_i \widetilde{u}_j + \overline{p}\, \delta_{ij} - \overline{\tau}_{ij} + \tau_{ij}^{sgs}] \\
\frac{\partial \overline{\rho} \widetilde{E}}{\partial t} &= -\frac{\partial}{\partial x_i}[(\overline{\rho} \widetilde{E} + \overline{p}) \widetilde{u}_i + \overline{q}_i - \widetilde{u}_j \overline{\tau}_{ji} + H_i^{sgs} + \sigma_{ij}^{sgs}]
\end{aligned} \tag{18}$$

where, $\widetilde{u}_i$ is the velocity, $\overline{p}$ is the pressure, $\overline{\tau}_{ij}$ is the viscous stress tensor, $\widetilde{E}$ is the total energy and $\overline{q}_i$ is the heat conduction term. The subgrid terms resulting from the filtering operation represent the small-scale

effects on the resolved scales in the form of additional stresses and fluxes. The subgrid terms that require closure are:

$$\begin{aligned} \tau_{ij}^{sgs} &= \overline{\rho}[\widetilde{u_i u_j} - \widetilde{u}_i \widetilde{u}_j] \\ H_i^{sgs} &= \overline{\rho}[\widetilde{E u_i} - \widetilde{E}\widetilde{u}_i] + [\overline{p u_i} - \overline{p}\widetilde{u}_i] \\ \sigma_i^{sgs} &= [\overline{u_j \tau_{ij}} - \widetilde{u}_j \overline{\tau}_{ij}]. \end{aligned} \tag{19}$$

The simplest models for the subgrid terms are eddy viscosity type of models of the form $\tau_{ij}^{sgs} - \frac{\delta_{ij}}{3}\tau_{kk} = -2\nu_t \overline{S}_{ij}$, which relates the subgrid scale stresses τ_{ij}^{sgs} to the large scale strain-rate tensor $\widetilde{S}_{ij} = \frac{1}{2}(\frac{\partial \widetilde{u}_i}{\partial x_j} + \frac{\partial \widetilde{u}_j}{\partial x_i})$. Here, ν_t is the eddy viscosity which is the unknown term.

One of the first approaches to determine the eddy viscosity coefficient was introduced by Smagorinsky,[15] as $\nu_\tau = C_s \bar{\triangle}^2 |S|$. Here, C_s is the Smagorinsky coefficient, $\bar{\triangle}$ is the filter width which can be computed as $\bar{\triangle} = (\triangle x_1 \triangle x_2 \triangle x_3)^{1/3}$ and $|S| = 2(\widetilde{S}_{ij}\widetilde{S}_{ij})^{1/2}$ is the large-scale strain rate tensor.

Another approach to determine the eddy viscosity is based on the subgrid kinetic energy, which is used to obtain the velocity scale. The general form of the K-eqn can be cast in the form

$$\frac{\partial \overline{\rho}\, k^{sgs}}{\partial t} + \frac{\partial}{\partial x_i}(\overline{\rho}\, \widetilde{u}_i k^{sgs}) = P^{sgs} - D^{sgs} + \frac{\partial}{\partial x_i}\left(\overline{\rho}\, \frac{\nu_t}{\sigma_K} \frac{\partial k^{sgs}}{\partial x_i}\right) \tag{20}$$

Here, P^{sgs} and D^{sgs} are the production and dissipation of k^{sgs}, respectively. The production term is defined as, $P^{sgs} = -\tau_{ij}^{sgs}(\frac{\partial \widetilde{u}_i}{\partial x_j})$, where τ_{ij}^{sgs} is the modeled subgrid stress tensor, $\tau_{ij}^{sgs} = -2\overline{\rho}\nu_t(\widetilde{S}_{ij} - \frac{1}{3}\widetilde{S}_{kk}\delta_{ij}) + \frac{2}{3}\overline{\rho}k^{sgs}\delta_{ij}$. Here, $\nu_t = C_\nu \overline{\Delta}(k^{sgs})^{1/2}$ is the eddy viscosity The dissipation term is modeled as $D^{sgs} = C_\epsilon \overline{\rho}(k^{sgs})^{\frac{3}{2}}/\overline{\Delta}$

The coefficients C_ν, C_ϵ can be evaluated based on the turbulence theory as $C_\nu = 0.067$ and $C_\epsilon = 0.916$ or adjusted dynamically as part of the solution using a localized dynamic procedure for the subgrid kinetic energy (LDKM).[16,17] In the current study, we follow the latter approach and obtain these coefficients using a scale similarity model. Although the details of the LDKM are given elsewhere, for completeness, we summarize the key features of the model here.

Dynamic procedure is based on the experimental free jet studies by Liu *et al.*,[18] where it has been suggested that the subgrid stress τ_{ij}^{sgs} at the grid filter level $\overline{\Delta}$ and the Leonard's stress L_{ij} at the test filter level $\widehat{\Delta}(= 2\overline{\Delta})$ are self-similar. In the LDKM model, this observation is further extended for the subgrid stress $\widehat{\tau}_{ij}^{sgs}$ at the test filter level. Thus, using scale similarity approach, the model coefficient C_ν is obtained as:

$$C_\nu = \frac{L'_{ij} M_{ij}}{2 M_{ij} M_{ij}} \tag{21}$$

In the above expression $L'_{ij} = L_{ij} - \frac{2}{3}\widehat{\overline{\rho}}\, k_{test}\delta_{ij}$ where, $L_{ij} = -2\widehat{\overline{\rho}} C_\nu \sqrt{k_{test}}\widehat{\Delta}(\langle \tilde{S}_{ij}\rangle - \frac{1}{3}\langle \tilde{S}_{ij}\rangle \delta_{ij}) + \frac{2}{3}\widehat{\overline{\rho}}\, k_{test}\delta_{ij}$ and $M_{ij} = -\widehat{\overline{\rho}}\, \sqrt{k_{test}}\widehat{\Delta}(\langle \tilde{S}_{ij}\rangle - \frac{1}{3}\langle \tilde{S}_{ij}\rangle \delta_{ij})$.

A similar approach is used to obtain the dissipation coefficient C_ε such that

$$C_\epsilon = \frac{\widehat{\Delta}\mu'}{\widehat{\overline{\rho}}\, k_{test}^{3/2}}(\langle \tau_{ij}^{sgs} \frac{\partial u_i}{\partial x_j}\rangle - \langle \overline{\tau}_{ij}^{sgs}\rangle \langle \frac{\partial u_i}{\partial x_j}\rangle) \tag{22}$$

where μ' is the total viscosity, defined as $\mu' = \mu + \mu_t$. Here, μ is the molecular viscosity and μ_t is the eddy viscosity at the grid filter level.

C. Relationship between TLS and LES approaches

The solution of the LES equations is obtained at discrete points, therefore, in LES, in addition to the explicit filter an implicit projection of the flow field $\tilde{u}_i$ is used that makes it possible to represent the field on a finite grid. Similar to implicit LES, in the TLS approach the large scale momentum $(\rho u_i)^L$ represents not only the filtered quantity but also the large scale momentum at LS grid points. Although its interpretation is different, the LS Eqs. (12) have the same form as the filtered LES Eqs. (18). These equations can be written

in a different equivalent form to show the similarities between the subgrid terms in the LES equations and small-scale interaction terms in the TLS equations as follows:

$$\begin{aligned}
\frac{\partial \rho^L}{\partial t} &= -\frac{\partial}{\partial x_i}(\rho u_i)^L \\
\frac{\partial}{\partial t}(\rho u_i)^L &= -\frac{\partial}{\partial x_j}\left[(\rho u_i)^L u_j^L + p^L \delta_{ij} - \tau_{ij}^L + \hat{\tau_{ij}^L}\right]^L \\
\frac{\partial}{\partial t}(\rho E)^L &= -\frac{\partial}{\partial x_i}\left[(\rho E)^L u_i^L + (p^L u_i^L)^L + q_i^L - (\tau_{ij}^L u_j^L)^L + \hat{H_i}^L + \hat{\sigma_i}^L\right]^L
\end{aligned} \tag{23}$$

In the direct simulation of the subgrid turbulence, the scale interaction terms are calculated directly from SS and LS fields. The LS part of the scale interaction stress is:

$$\hat{\tau_{ij}}^L = \left[(\rho u_i) u_j\right]^L - \left[(\rho u_i)^L u_j^L\right]^L = \left[(\rho u_i)^L u_j^S + (\rho u_i)^S u_j^L + (\rho u_i)^S u_j^S\right]^L \tag{24}$$

Similarly, the LS part of the scale interaction enthalpy flux:

$$\begin{aligned}
\hat{H_i}^L &= \left[(\rho E) u_i\right]^L - \left[(\rho E)^L u_i^L\right]^L + \left[(p u_i) - (p^L u_i^L)\right]^L \\
&= \left[(\rho E)^L u_i^S + (\rho E)^S u_i^L + (\rho E)^S u_i^S\right]^L + \left[p^L u_i^S + p^S u_i^L + p^S u_i^S\right]^L
\end{aligned} \tag{25}$$

The LS part of the scale interaction viscous work:

$$\hat{\sigma_i}^L = (\tau_{ij} u_j)^L - (\tau_{ij}^L u_j^L)^L = \left[\tau_{ij}^L u_j^S + \tau_{ij}^S u_j^L + \tau_{ij}^S u_j^S\right]^L \tag{26}$$

The small scale interaction terms $\hat{\tau_{ij}}^L$, $\hat{H_i}^L$ and $\hat{\sigma_i}^L$ are closed if the small scale field is known which can be obtained by solving the SS Eqs. (14) defined in the TLS formulation.

This formulation shows that LES equations can also be obtained from the TLS methodology without applying any kind of filtering. The scale interaction terms in the TLS formulation and the subgrid terms in the LES formulation are both similar, which proves that the subgrid terms in the LES equations can be directly calculated from the TLS equations without using any eddy viscosity model.

D. Near-wall coupled TLS-LES model

Near-wall TLS-LES approach is based on direct modeling of the subgrid stresses near the wall region with the TLS model and using traditional LES modeling for the bulk flow. The TLS evolution equations for SS are solved only in the inner region and boundary conditions must be applied at the physical boundaries. The wall-normal TLS lines begin at the no-slip wall ($y = 0$) and extend up to the edge of the near-wall region ($y = Y$) (Fig. 3). At $y = Y$, two boundary conditions have been evaluated: the first one is a zero gradient boundary condition for the small scale velocities and the second one is the direct calculation of the small scale velocities in terms of the local subgrid kinetic energy k^{sgs} (obtained from the K-eqn (Eq. 20)). This approach assumes that small scales are isotropic at the edge of the inner region.

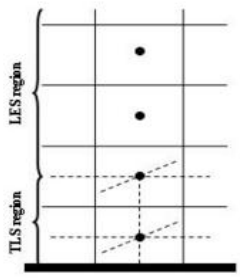

Figure 3. Illustration of Near-wall TLS-LES model.

Boundary conditions at $y = 0$:

$u_i^s = 0,\ i = 1, 2, 3$

and at $y = Y$:

Zero gradient boundary condition $\quad \partial u_i^s / \partial y = 0, \quad i = 1, 2, 3$

or fluctuating boundary condition $\quad u_i^s = \sqrt{\frac{2}{3} k^{sgs}} W_i, \quad i = 1, 2, 3$

where W_i is a random number with zero mean. The wall-normal TLS lines can also be extended to another LES cell to improve the boundary condition for the small scale equation in the overlapping region.

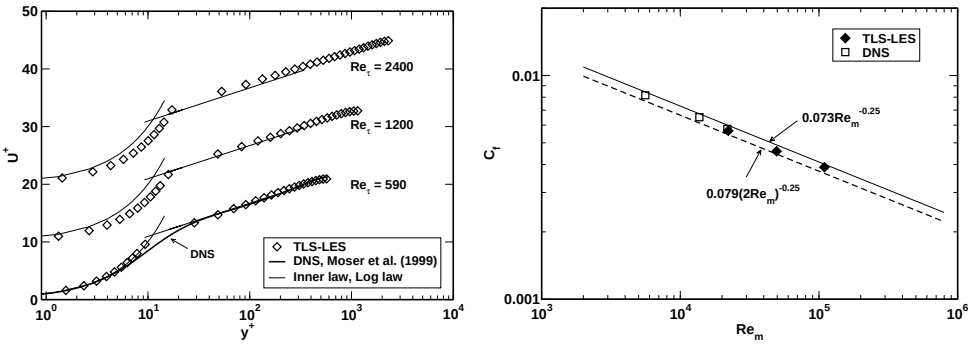

(a) Mean velocity $\langle U^+ \rangle$ (b) Friction coefficient C_f

Figure 4. Near-wall TLS-LES mean quantities.

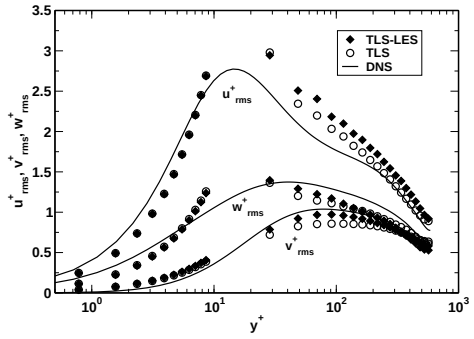

Figure 5. RMS velocity fluctuation profiles for $Re_\tau = 590$ computed from TLS-LES, pure TLS and DNS.[19]

III. Results and Discussion

A. Turbulent Channel Flow

The fully developed channel flow has been widely studied in the past, and both experimental and DNS data are available for comparison purposes. Pure TLS results of Kemenov and Menon[11,12] show the capability of the model for capturing the near-wall flow energetics of 3D turbulent flow. Here, we present the results based on the new near-wall TLS-LES approach.

The fully developed channel flow of width $2h$, where h is the channel half-width, is simulated by applying periodic boundary conditions in the stream-wise and span-wise directions and no-slip conditions in the cross-stream direction. Calculations are performed for Reynolds numbers based on friction velocities of 590, 1200

Table 1. Simulation parameters and mean flow variables for TLS-LES channel flow simulations

	Grid	Re_τ	$\triangle y^{+SS}$	$\triangle y^{+LS}$	C_f
DNS[19]	$384 \times 257 \times 384$	590		0.042	$5.76\text{x}10^{-3}$
TLS-LES	$32 \times 40 \times 32$	590	1.067	9.395	$5.66\text{x}10^{-3}$
TLS-LES	$32 \times 40 \times 32$	1200	1.320	15.861	$4.58\text{x}10^{-3}$
TLS-LES	$64 \times 50 \times 64$	2400	1.436	17.041	$3.89\text{x}10^{-3}$

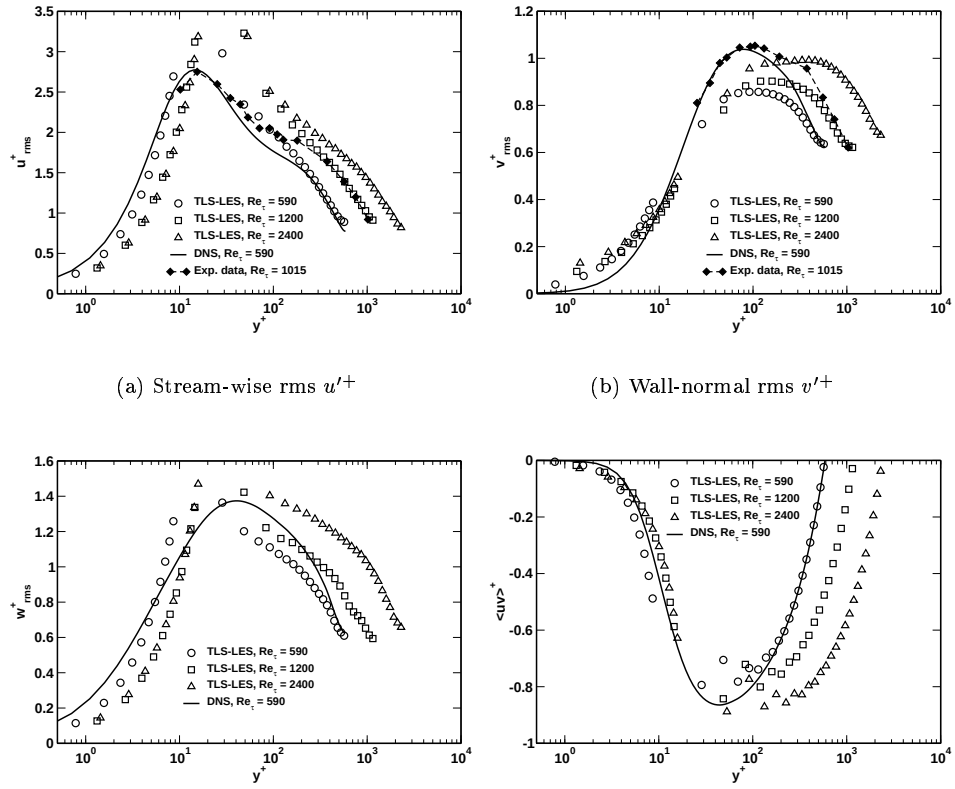

(a) Stream-wise rms u'^+

(b) Wall-normal rms v'^+

(c) Span-wise rms w'^+

(d) Reynolds stress

Figure 6. Near-wall TLS-LES rms quantities.

and 2400. Near-wall TLS-LES results for statistically steady flow are compared to Moser's[19] DNS data for $Re_\tau = 590$ and Wei's[20] experimental data for $Re_\tau = 1200$. Here $Re_\tau = u_\tau h/\nu$, where $u_\tau = \sqrt{\nu du/dy|_{y=0}}$ is the friction velocity.

The computational domain is discretized by $32 \times 40 \times 32$ LS grid cells for $Re_\tau = 590$ and $Re_\tau = 1200$ with uniform grid in the periodic directions (streamwise and spanwise) and nominal stretched grid in the wall normal direction. As the Reynolds number increases, only a smaller portion of kinetic energy can be captured on the LS grid. Thus, for the high Reynolds number ($Re_\tau = 2400$) case, the resolution was increased to $64 \times 50 \times 64$. In all cases, a uniform grid of 8 SS cells per LS cell is used in the periodic directions and a variable grid of 10 to 12 is used in the wall normal direction. The near-wall region for TLS-LES are represented by three LS cells extending up to $y^+ \approx 50$ ($y^+ = yu_\tau/\nu$). The near-wall SS grid spacing is kept approximately $y^+ \approx 1$. The standard LES with dynamic Germano subgrid model is used in the outer region. The simulation parameters and the mean flow variables are given in Table 1.

Figure 4 (a) presents the near-wall TLS-LES results for the mean velocity profiles over the Reynolds-number range indicated in Table 1. For $Re_\tau = 590$ the DNS data of Moser[19] is used for direct comparison. For all cases, the inner law $u^+ = y^+$, and log law, $u^+ = 2.44lny^+ + 5.2$, is also plotted for comparison. Near-wall TLS-LES model predicts slightly higher values in the buffer region ($10 < y^+ < 30$) for $Re_\tau = 590$ which might be caused by the coarse LS grid (which was chosen deliberately as a worst case scenario). The overall mean velocities are predicted quite well with the near-wall TLS-LES model. At all Reynolds numbers, the physically realistic viscous sublayer is captured reasonably well.

Figure 4 (b) shows the computed skin friction coefficients compared with the DNS data of Moser[19] and the turbulent correlation of Dean.[21] The Reynolds number used in this plot is based on the bulk velocity and the channel width, and the friction coefficient is defined as $C_f = 2(u_\tau/U_{ref})^2$. Good agreement is obtained with the DNS C_f value at $Re_\tau = 590$. Overall, the friction coefficient demonstrates the right trend.

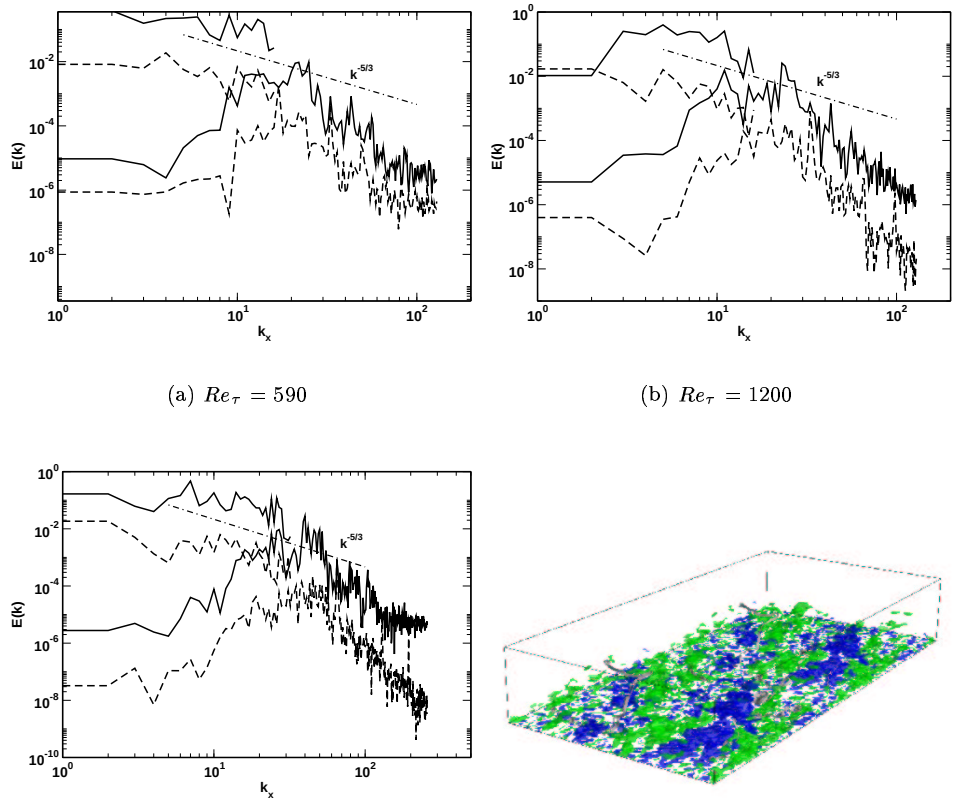

(a) $Re_\tau = 590$ (b) $Re_\tau = 1200$

(c) $Re_\tau = 2400$ (d) $Re_\tau = 2400$

Figure 7. Near-wall TLS-LES calculations: (a-c) Instantaneous (solid lines) and volume averaged (dashed lines) stream-wise spectra; (d) Isosurfaces of the streamwise velocity fluctuations: $u' = +3$ (blue) and $u' = -3$ (green).

Figures 5 and 6 show the rms velocity fluctuations predicted by the near-wall TLS-LES model. In Fig. 5 near-wall TLS-LES computed rms velocity fluctuation profiles for $Re_\tau = 590$ are compared with the DNS calculations of Moser[19] and results obtained by pure TLS calculations. TLS based models (pure TLS and near-wall TLS-LES) correctly predict the location and the peak value of the streamwise rms-velocity fluctuation for $Re_\tau = 590$, but produce a broader profile. However, the near-wall TLS-LES model underpredicts the rms-velocity fluctuations compared to the pure TLS result in the bulk flow. This is due to the highly dissipative behavior of the Germano model, which is used for the LES bulk flow computations. We plan to revisit this with the one-equation model for the subgrid kinetic energy[16,17] later.

In Fig. 6, near-wall TLS-LES results for rms-velocity fluctuations are compared to the DNS result of Moser[19] and the data of Wei.[20] For two high Reynolds cases u^+_{rms} lead to very similar results, demonstrating universality of flow properties close to the wall at high Reynolds numbers.

Figures 7 (a), (b) and (c) show instantaneous streamwise energy spectra. 1D-line and plane-averaged spectra are plotted and compared to the slope of $k^{-5/3}$. It can be seen that the near-wall TLS-LES approach recovers both LS and SS spectras. Finally, high and low-speed streaks, shown in Fig. 7 (d) for $Re_\tau = 2400$ for near-wall TLS-LES case, exhibit a typical near-wall pattern.

Overall trend of the TLS-LES results show the capabilities of the proposed model for near-wall applications using relatively coarse grids.

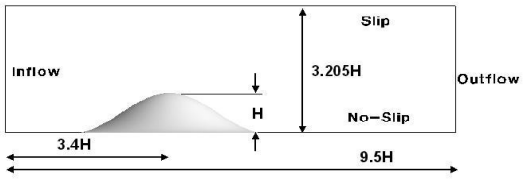

Figure 8. Geometry.

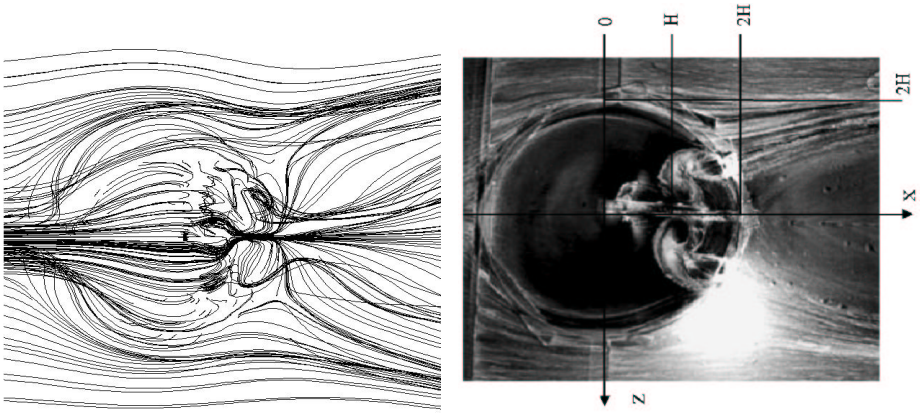

(a) Predicted with near-wall TLS-LES (b) Experiments

Figure 9. Oil-flow visualizations and instantaneous streamlines in the near-wall region.

B. Three Dimensional Flow over an Axisymmetric Hill

To show the capability of the proposed model for complex geometries, a three-dimensional boundary layer flow, investigated experimentally by Simpson *et al.*,[22] is chosen. This flow involves three-dimensional unsteady separation and reattachment. High Reynolds number of this types of flows are of considerable interest because of their relevance to practical flows. In one of the recent study,[23] LES with the LDKM subgrid model have been applied to the same flow and complex flow pattern was predicted quite well. In this study LES using LDKM subgrid model is revisited for completeness. The results are compared with Simpson *et al.*'s[22] experimental data. Then, this flow is simulated with the near-wall TLS-LES model.

Figure 8 presents the geometry of the configuration in the streamwise and wall-normal directions. The hill height is $H = 0.078m$ with the circular base of radius $R = 2H$. The zenith of the hill is about $3.4H$ downstream from the inflow boundary. The computational domain extends $10.0H$ in the spanwise and $9.5H$ in the streamwise direction. The shape of the hill is defined as $y(r)/H = -1/6.04844[J_o(\Lambda)I_o(\Lambda r/R) - I_o(\Lambda)J_o(\Lambda r/R)]$ where $\Lambda = 3.1926$, J_o and I_o are the Bessel and modified Bessel function of the first kind, respectively. The Reynolds number based on height H and inflow velocity (U_{ref}=27.5 m/s), is approximately 130,000.

The computational domain is discretized with $192 \times 184 \times 144$ grid points, with a small stretching in the wall normal region and on the lee-side of the hill for LES-LDKM case. For this grid the minimum grid resolution in the wall-normal direction is about $y = 56\mu m$. The minumum grid resolution is estimated as $(\Delta x^+, \Delta y^+, \Delta z^+) = (100, 4, 120)$ in terms of viscous wall units. For near-wall TLS-LES case, relatively coarse grid compared to full LES case is used. The computational domain is discretized by $48 \times 46 \times 36$ LS grid cells. The SS resolution for streamwise lines is 385, for spanwise lines 289 and for wall normal lines 51. The near-wall region for bottom wall is represented by five LS cells extending up to $y^+ \approx 40$. The near-wall grid spacing for LS is $y = 188\mu m$ and for SS is $y = 15.6\mu m$ in the wall-normal direction.

At the lower wall, no-slip conditions are enforced for velocity and k^{sgs}, whereas at the upper wall,

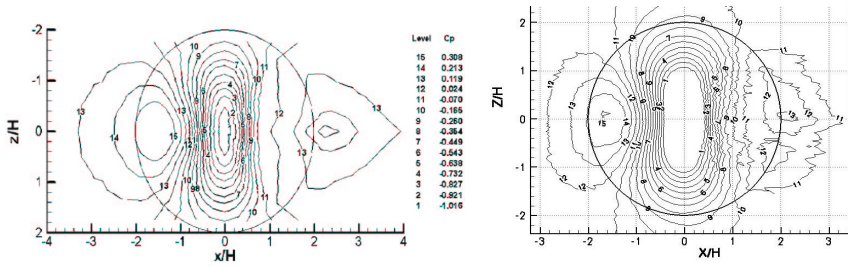

(a) Experimental C_p

(b) Predicted C_p with LES-LDKM

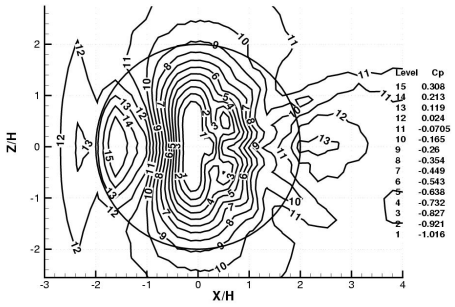

(c) Predicted C_p with near-wall TLS-LES

Figure 10. Static-pressure coefficient contours over the hill surface.

slip boundary conditions are enforced. At the outlet, characteristic boundary conditions are applied to all variables. For near-wall TLS-LES case, initial LS velocity field was determined from the full LES-LDKM flow field.

Figure 9 presents a comparison of the predicted surface streamline pattern with the experimental oil-flow pattern. Based on surface streamline patterns, the flow on the lee side of the bump is very complex and shows 3D separation and reattachment because of both streamwise and spanwise pressure gradients on the lee side. Qualitative agreement is found between the near-wall TLS-LES results and experimental oil flow visualization.

Figure 10 presents the computed surface distribution of static pressure coefficients (C_p) and the corresponding experimental result. There is a good similarity in both features and magnitudes between the LES-LDKM computation and the experimental data. In the spanwise direction, both LES-LDKM and experiments show a symmetric pressure distribution. Figure 10 (c) presents the near-wall TLS-LES model results for the pressure coefficient. It is clear from this figure that the near-wall TLS-LES is capable of predicting approximately the correct pressure distribution around the bump. There are some discrepancies in the lee side where the flow is separating and this is an issue to be addressed in the future. Both results show that as the boundary layer approaches the leading edge of the hill the pressure increases. The pressure then decreases at the zenith of the hill as the flow accelerates over the hill. The position of minumum pressure is predicted accurately by all (LES-LDKM and near-wall TLS-LES) simulations.

Wake measurements are performed at $3.69H$ downstream of the zenith hill, where the flow has reattached on the wall and turbulent boundary layer has reformed. Figure 11 presents a comparison for time-averaged streamwise and spanwise velocities at $3.69H$ for various spanwise locations. LES-LDKM and near-wall TLS-LES results are compared with the experimental data. All models overpredict the streamwise velocity, which can be related to the coarser spatial resolution used away from the wall. However, cross-stream velocity profiles are well predicted with LES-LDKM and near-wall TLS-LES models as shown in Fig. 11 (b). From Fig. 11, overall agreement between predictions and experiments is reasonable.

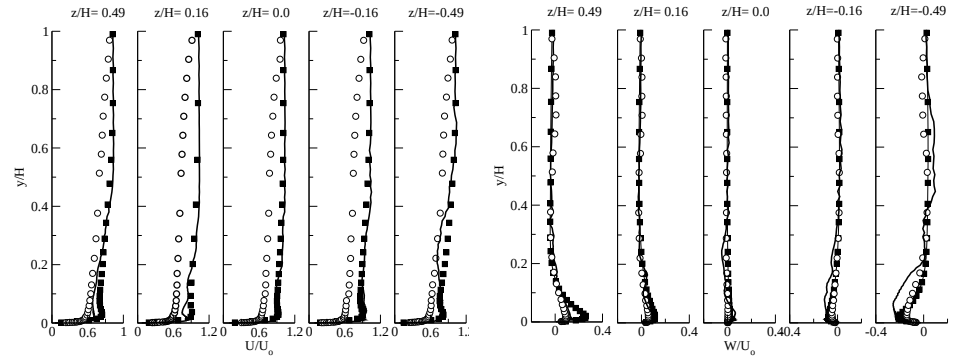

(a) U/U_{ref} (b) W/U_{ref}

Figure 11. Mean flow quantities predicted by LES-LDKM (solid lines) and near-wall TLS-LES model (square symbols).

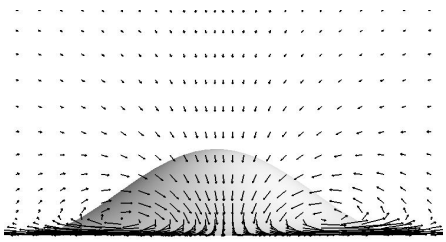

Figure 12. Secondary flow vector field predicted with near-wall TLS-LES model.

Figure 12 shows the instantaneous secondary flow vector field predicted with near-wall TLS-LES model at $x/H = 3.69$ plane. The presence of streamwise counter-rotating vortex pair, located at $y/H = 0.2$, is observed, which is consistent with the observations of Perrson *et al.*[24]

Snapshots of the LS and SS vorticity magnitude isosurfaces at a level of $|\overline{w}^L| = 1100$ and $|\overline{w}^S| = 300$ are shown in Fig. 13. Isosurfaces are colored with local spanwise velocity. It is seen that the simulated SS field responds to the LS field by creating fine scale SS field at the high gradient LS regions.

Current results show the capability of LES, using LDKM subgrid model, for complex flows. The near-wall TLS-LES of this flow shows qualitative agreement with the experimental and LES results. Overall results looks reasonable for this kind of coarse resolution. A finer resolution is expected to provide better results and will be adressed in the near future.

IV. Conclusion

The resolution requirement to predict real flow features near a no-slip wall limits LES and DNS to relatively low Reynolds numbers. To overcome this resolution requirement, a new model is proposed in this paper. TLS model is applied as a subgrid closure for LES equation near the wall. This proposed model is applied to fully developed turbulent channel flow. Results of the near-wall TLS-LES channel flow suggests that near-wall implementation of TLS may be a viable alternative subgrid model for LES of wall bounded flows. In this simulation, dynamic Smagorinsky model by Germano is used as a subgrid closure for LES bulk flow region. Germano model has some limitations in conventional LES models and these limitations remain in the near-wall TLS-LES approach. It is believed that using localized dynamic one equation model (LDKM)[16,17] in the bulk flow region as a subgrid closure will improve the solutions. A three-dimensional turbulent boundary layer flow is simulated to analyze the LDKM subgrid model. Results show

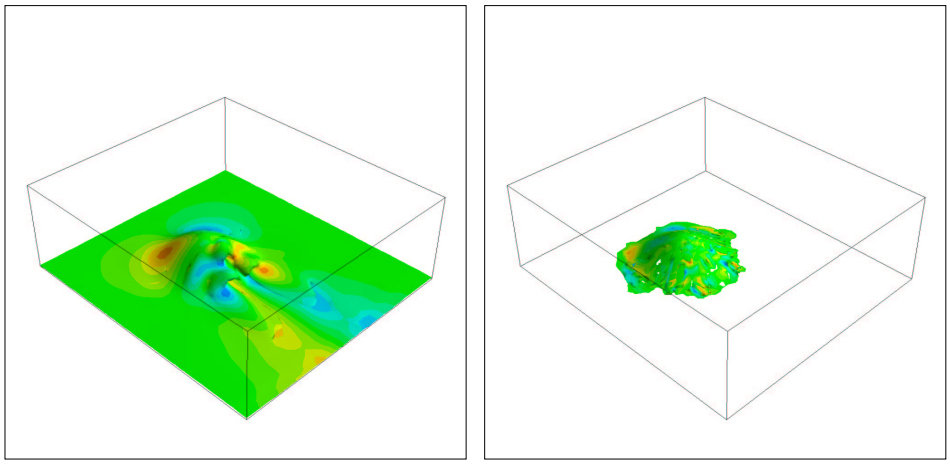

(a) LS (b) Resolved SS

Figure 13. Instantaneous LS (a) and resolved SS (b) vorticity magnitude isosurfaces predicted with near-wall TLS-LES model. Isosurfaces are colored with local spanwise velocity.

good agreement with the experimental data. Then TLS-LES is used as a near-wall subgrid closure model for high-Re number wall bounded flows past a three-dimensional bump. Overall results show the capability of the model for high Reynolds number complex flows using very coarse grids. The statistical analysis of this complex flow and further investigations of small-scale equation model assumptions for separated flows are the subject of future studies.

V. Acknowledgment

This work is supported by the Office of Naval Research. Computational time provided by DOD HPC at NAVOCEANO, ERDC and ARL are gratefully acknowledged.

References

[1]Fureby, C., Alin, N., Wikstrom, N., Menon, S., Svanstedt, N., and Persson, L., "On Large Eddy Simulation of High Reynolds Number Wall Bounded Flows," *AIAA Journal*, Vol. 42, 2004, pp. 457–469.

[2]Baggett, J. S., Jimenez, J., and Kravchenko, A. G., "Resolution Requirements in Large-Eddy Simulations of Shear Flows," *Center For Turbulent Research, Annual Research Briefs*, 1997, pp. 51–66.

[3]Piomelli, U. and Balaras, E., "Wall layer models for large eddy simulation," *Annual Review of Fluid Mechanics*, Vol. 34, 2002, pp. 349–374.

[4]Cabot, W. and Moin, P., "Approximate wall boundary conditions in the large-eddy simulation of high Reynolds number flow," *Flow Turb. Combust.*, Vol. 63, 1999, pp. 269.

[5]Kemenov, K. and Menon, S., "Explicit small-scale velocity simulation for high-Re turbulent flows," *to appear in Journal of Computational Physics*, 2006.

[6]Hughes, T., Mazzei, L., and Oberai, A., "The multiscale formulation of Large-eddy simulation: Decay of homogeneous isotropic turbulence," *Physics of Fluids*, Vol. 13, No. 2, 2001, pp. 505–512.

[7]Hughes, T., Oberai, A., and Mazzei, L., "Large eddy simulation of turbulent channel flows by variational multiscale method," *Physics of Fluids*, Vol. 13, No. 6, 2001, pp. 1784–1799.

[8]Dubois, T., Jauberteau, F., and R., T., "Dynamic multilevel methods and the numerical simulation of turbulence," Cambridge University Press, 1999.

[9]Laval, J., Dubrule, B., and Nazarenko, S., "Nonlocality of interaction of scales in the dynamics of 2D incompressible fluids," *Phys.Rev.Let*, Vol. 83, 1999, pp. 4061–4064.

[10]Laval, J., Dubrule, B., and Nazarenko, S., "Nonlocality and intermittency in three-dimensional turbulence," *Physics of Fluids*, Vol. 13, 2001, pp. 1995–2012.

[11]Kemenov, K. and Menon, S., "A Two-Level Simulation Methodology for LES of High Reynolds Number Flows," *Advances in Turbulence IX*, CIMNE, 2002, pp. 203–206.

[12]Kemenov, K. and Menon, S., "Two level simulation of high-Re number non-homogeneous turbulent flows," *AIAA paper 2003-0084*, 2003.

[13]Kemenov, K. and Menon, S., "Two Level Simulation of High-Re Turbulent Flows," *Direct and Large-Eddy Simulations V*, Kluwer, 2003.

[14]Kemenov, K., Gungor, A., and Menon, S., "Two Level Simulation of High-Re Wall Bounded FLows and Isotropic Turbulence," *AIAA paper 2005-5318*, 2005.

[15]Smagorinsky, J., "General Circulation Experiments with the Primitive Equations," *Monthly Weather Review*, Vol. 91, No. 3, 1993, pp. 99–164.

[16]Menon, S. and Kim, W.-W., "High Reynolds number flow simulations using the localized dynamic subgrid-scale model," *AIAA Paper 96–0425*, 1996.

[17]Kim, W.-W. and Menon, S., "An unsteady incompressible Navier-Stokes solver for Large-Eddy Simulation of turbulent flows," *International Journal of Numerical Fluid Mechanics*, Vol. 31, 1999, pp. 983–1017.

[18]Liu, S., Meneveau, C., and Katz, J., "On the Properties of Similarity Subgrid-Scale Models as Deduced from Measurements in a Turbulent Jet," *Journal of Fluid Mechanics*, Vol. 275, 1994, pp. 83–119.

[19]Moser, R., Kim, J., and Mansour, N., "Direct numerical simulation of turbulent channel flow up to $Re_\tau = 590$," *Physics of Fluids*, Vol. 11, 1999, pp. 943–945.

[20]Wei, T. and Willmarth, W., "Reynolds-number effects on the structure of a turbulent channel flow," *Journal of Fluid Mechanics*, Vol. 204, 1989, pp. 57.

[21]Dean, R. B., "Reynolds number dependence of skin friction and other bulk flow variables in two-dimensional rectangular duct flow," *Journal of Fluids Engineering*, Vol. 100, 1978, pp. 215–228.

[22]Simpson, R., Long, C., and Byun, G., "Study of vortical separation from an axisymmetric hill," *International Journal of Heat and Fluid Flow*, Vol. 23, 2002, pp. 582–591.

[23]Patel, N. and Menon, S., "Large-Eddy Simulations of Turbulent Flow over an Axisymmetric Bump," *AIAA paper 2003-0967*, 2003.

[24]Persson, T., Liefvendahl, M., Bensow, R., and Fureby, C., "Numerical investigation of the flow over an axisymmetric hill using LES, DES, and RANS," *Journal of Turbulence*, Vol. 7, No. 4, 2006, pp. 1–17.